IEEE Access
Multidisciplinary ⋮ Rapid Review ⋮ Open Access Journal

Received 3 December 2023, accepted 9 December 2023, date of publication 13 December 2023,
date of current version 20 December 2023.

Digital Object Identifier 10.1109/ACCESS.2023.3342710

RESEARCH ARTICLE

Probability Mass Function-Based Adaptive Median Filtering for Acoustic Radiation Force Impulse Imaging: A Feasibility Study

GA YEONG LEE, (Student Member, IEEE), GYU LI RA, (Student Member, IEEE), GIL SU KIM, (Student Member, IEEE), HAK HYUN MOON, (Student Member, IEEE), AND JONG SEOB JEONG, (Member, IEEE)

Department of Biomedical Engineering, Dongguk University, Seoul 04620, South Korea

Corresponding author: Jong Seob Jeong (jjsspace@dongguk.edu)

This work was supported in part by the Korea Medical Device Development Fund Grant funded by the Korean Government (the Ministry of Science and ICT, the Ministry of Trade, Industry and Energy, the Ministry of Health and Welfare, and the Ministry of Food and Drug Safety) under Project RS-2022-00141273; in part by the National Research Foundation (NRF) funded by the Korean Government under Grant 2021R1A2C1004329; and in part by the 2022 Dongguk University Research Fund.

ABSTRACT Among ultrasound images, the acoustic radiation force impulse (ARFI) image can provide information about the stiffness of the tissue using both a pushing beam and a detection beam. However, there is a problem in that the impulse noise is generated in the process of generating the ARFI image by calculating the displacement of the target. The impulse noise appearing in the ARFI image can be caused by various factors related to ultrasound image processing and the characteristics of the target tissue, and it can degrade image quality and the accuracy of stiffness measurements. The commonly used fixed median filter in the ARFI image can effectively eliminate the impulse noise but may introduce a blurring effect, depending on the kernel size. The adaptive median filter has the advantage of minimizing the impulse noise level while preserving the original information as much as possible, but the adaptive median filter has been generally used to remove the unipolar or bipolar type noise from the image. As a result, the effectiveness of removing the impulse noise with various amplitudes from the ARFI image is not sufficient. To figure out this problem, in this study, we propose the adaptive median filter method combined with probability mass function. In this method, in order to limit the various amplitudes of impulse noise as much as possible, the threshold cut-off level of impulse noise is determined by a probability mass function, and then adaptive median filter is used to effectively remove impulse noise with limited amplitude. The performance of the proposed method was evaluated by using a tissue mimicking phantom and a bovine eye. Therefore, the proposed technique is expected to be one of the useful methods to improve the overall quality and reliability of the ARFI images for clinical diagnosis and evaluation.

INDEX TERMS Acoustic radiation force impulse image, probability mass function, fixed median filter, adaptive median filter, impulse noise.

I. INTRODUCTION

The acoustic radiation force impulse (ARFI) imaging has demonstrated its usefulness in diagnosing benign and malignant tumors in various human organs such as liver, prostate, kidney, thyroid, and breast [1], [2], [3], [4], [5], [6]. The ARFI can estimate tissue displacement used for local strain calculation based on the cross-correlation between pre- and post-compressed echo signals generated by the external force [6], [7]. It is well known that decorrelation error occurs during the displacement estimation when using the cross-correlation process [8], [9], [10], [11]. In other words, it is not possible to accurately estimate the time delay between echo signals before compression and after compression due

The associate editor coordinating the review of this manuscript and approving it for publication was Riccardo Carotenuto.

to physical issues such as tissue scattering shift, tissue compression, non-rigid tissue deformation, slide-slippage, and out-of-plane motion. This artifact reduces the signal-to-noise ratio (SNR) and the dynamic range of the image [12], [13]. One of the critical noises caused by the decorrelation error is the false peak noise called impulse noise, and it affects the precise estimation of the displacement [14]. Additionally, the impulse noise in the form of the relatively large spike in displacement estimation is discontinuous in the displacement vector. This ultimately results in noisy images and poor estimation performance of displacement in the ARFI image [15], [16], [17].

A fixed median filter (FMF) has been widely used to remove the impulse noise artifacts. The main drawback of the FMF is that it removes fine image details by correcting all elements, including those that are not noisy [14], [15], [18]. Also, if the noise density is large, the noise cannot be sufficiently removed. Using a larger kernel size of the FMF will improve performance but make the image blurrier. An adaptive median filter (AMF) can solve these problems. Unlike the FMF, whose performance is determined by noise density, the performance of the AMF can be improved compared to the FMF because the kernel size of the AMF varies depending on the condition during the filtering process [16], [17], [18]. Also, AMF preserves the edges and fine details of the image by conditionally preserving all pixel values instead of replacing them all with their median values. However, the typical AMF has been shown to be effective against mainly unipolar or bipolar impulse noise. The AMF does not work well if the impulse noise has various amplitudes [19], [20], [21], [22], [23], [24], [25].

In order to figure out this issue, in this study, we propose the probability mass function based adaptive median filter (PMF_AMF). In this method, the optimal cut-off threshold level to separate the impulse noise from the true displacement of the target was derived from the probability mass function (PMF), and this process makes most impulse noise has unipolar or bipolar type amplitude. In other words, the amplitude of the impulse noise can be limited by using PMF. Then AMF was used to effectively remove the impulse noise. Also, unlike previous researches, all signal processing was conducted based on the radio frequency (RF) data rather than image files. The performance of the proposed method was evaluated by using a tissue mimicking phantom and a bovine eye. In Section II, the principle of the ARFI, the proposed PMF_AMF, and the experimental setup were illustrated, and Section III explained the experimental results. Discussion and Conclusion on the proposed technique were described in Section IV and Section V, respectively.

II. METHODS

A. PRINCIPLE OF ACOUSTIC RADIATION FORCE IMPULSE IMAGE

Among the several elastography techniques, the acoustic radiation force impulse (ARFI) imaging provides mechanical properties of the local tissue using the acoustic radiation

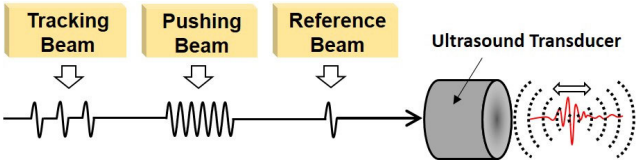

FIGURE 1. Schematic diagram of the beam sequence composed of a reference beam, a pushing beam, and a tracking beam for the ARFI imaging.

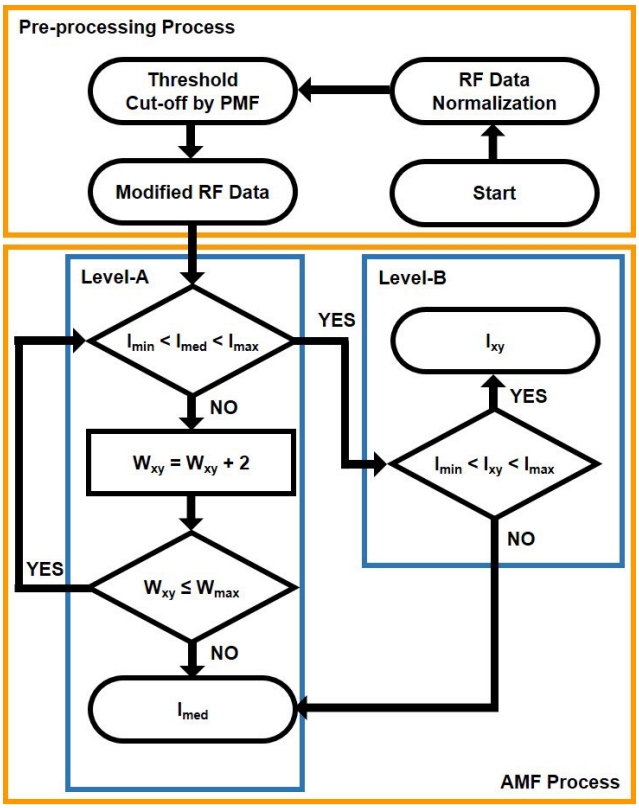

FIGURE 2. Flow chart of the proposed PMF_AMF technique composed of the pre-processing and the AMF processes. The AMF process consists of Level-A and Level-B steps.

force [26], [27], [28], [29], [30], [31], [32]. To implement ARFI imaging, as shown in Fig. 1, the tissue motion is generated by applying the pushing beam consisting of the high-intensity pulses with a long duration after sending the reference beam for motion detection. The tracking beam is then transmitted to obtain information about the local tissue displacement, which depends on the stiffness of the target. The displacement is quantitatively calculated using the received reference beam and the tracking beams, and the correlation-based method.

B. PROBABILITY MASS FUNCTION BASED ADAPTIVE MEDIAN FILTERING

In general, the amplitude of the impulse noise occurring in the ARFI image is large and non-uniform, and thus using the typical AMF as is does not work well in the ARFI image. To solve this issue, in this study, we propose PMF_AMF. In this method, the optimal cut-off threshold level to separate

the impulse noise from the true displacement of the target was derived from the PMF, and this process makes most impulse noise has limited amplitude. Subsequently, AMF was used to effectively remove the impulse noise.

Fig. 2 shows the flow chart of the proposed PMF_AMF technique, which consists of the pre-processing and the AMF processes. Also, the AMF process is composed of Level-A and Level-B steps. In the pre-processing process, the acquired ARFI RF echo data containing the target's displacement information is normalized to facilitate comparison of different displacement data sets. After deriving the PMF of the normalized data, the level of the sparse data is regarded as a noise and designated as a threshold. Choosing an appropriate threshold value is important for effective noise removal. Setting the threshold too aggressively can result in loss of important signal information, while too lenient can result in persistent noise.

After the pre-processing process, the modified RF data goes through the AMF process. In general, the AMF process operates separately as Level-A and Level-B steps. The Level-A step performs the spatial analysis of element intensities to detect an impulsive noise, while the Level-B step adjusts the filtering strategy based on the information provided by the Level-A step.

In the Level-A step, a kernel is generated around the center element (I_{xy}). The entered RF data within the kernel is sorted in ascending order by intensity value, identifying the largest value as I_{max}, the smallest value as I_{min}, and the median value as I_{med}. When the modified RF data enters, it checks if the condition $I_{min} < I_{med} < I_{max}$ is satisfied. If the value of I_{med} is same as to I_{min} or I_{max}, this condition is not met. In this case, the kernel size (W_{xy}) is increased to recheck the condition. If the kernel size is increased and becomes larger than the predefined maximum kernel size (W_{max}), the filter outputs I_{med}. In this case, it can be determined that more than half of the kernel is filled with I_{max} or I_{min}, and since I_{max} or I_{min} is determined to be the target information rather than impulse noise, I_{xy} is replaced with I_{med}. In other words, if I_{xy} has the same value as I_{med}, the data can be said to be maintained, and if I_{xy} has a specific value other than I_{max} or I_{min}, it is replaced by I_{med}. Thus, it eventually has a value similar to the surrounding elements.

Next, if the condition $I_{min} < I_{med} < I_{max}$ in the Level-A stage is satisfied, it indicates that I_{med} is within a reasonable range compared to the values of the surrounding elements, that is, there is a high probability that it is target information. Afterwards, in Level-B, you can determine whether the I_{xy} value is noise or information about the target through the condition $I_{min} < I_{xy} < I_{max}$. If this condition is met, it means that I_{xy} is within a reasonable range of the values of other nearby elements and is therefore likely to be the target's information. In this case, the filter concludes that I_{xy} is most likely not noise, and outputs I_{xy}. If I_{xy} does not meet the condition $I_{min} < I_{xy} < I_{max}$, there is a high possibility that I_{xy} is noise that is not within the reasonable value range of its neighbors, and I_{med} replaces I_{xy} to remove the noise. Subsequently, the final ARFI image can be implemented using the I_{med} and I_{xy} obtained in this way.

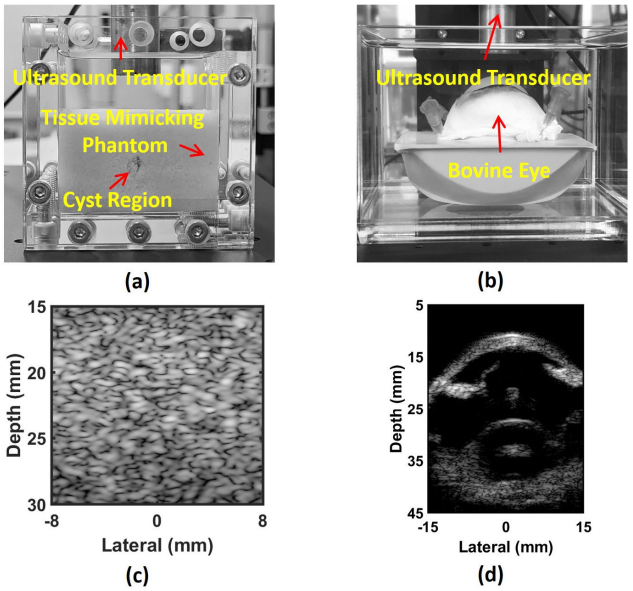

FIGURE 3. Photographs of targets and corresponding B-mode images: (a) tissue mimicking phantom and (b) bovine eye; (c) B-mode image of (a) and (d) B-mode image of (b).

C. PERFORMANCE EVALUATION METHODS

The performance of the proposed method was evaluated by a peak signal to noise ratio (PSNR) based on a mean squared error (MSE) in the below equation (1), (2).

$$\mathrm{MSE} = \frac{1}{n}\sum_{i=1}^{n}(Y_i - \hat{Y}_i)^2 \tag{1}$$

$$\mathrm{PSNR} = 10log\frac{s^2}{MSE} \tag{2}$$

Additionally, the structural similarity index measure (SSIM) in equation (3), a method of measuring similarity to the original image against distortion due to any transformation.

$$\mathrm{SSIM}\,(x, y) = [l\,(x, y)]^{\alpha}\cdot[c\,(x, y)]^{\beta}\cdot\left[s\,(x, y)\right]^{\gamma} \tag{3}$$

The SSIM index is composed of three terms such as the luminance term (equation (4)), the contrast term (equation (5)), and the structural term (equation (6)).
where

$$l\,(x, y) = \frac{2\mu_x\mu_y + C_1}{\mu_x^2 + \mu_y^2 + C_1} \tag{4}$$

$$c\,(x, y) = \frac{2\sigma_x\sigma_y + C_2}{\sigma_x^2 + \sigma_y^2 + C_2} \tag{5}$$

$$s\,(x, y) = \frac{\sigma_{xy} + C_3}{\sigma_x\sigma_y + C_3} \tag{6}$$

In this case, μ_x, μ_y, σ_x, σ_y, σ_{xy} are local means, standard deviations, and cross-covariance for images x, y. Since the initial image has the impulse noise, the performance evaluation was focused on the relative comparison between FMF, conventional AMF, and the proposed PMF_AMF.

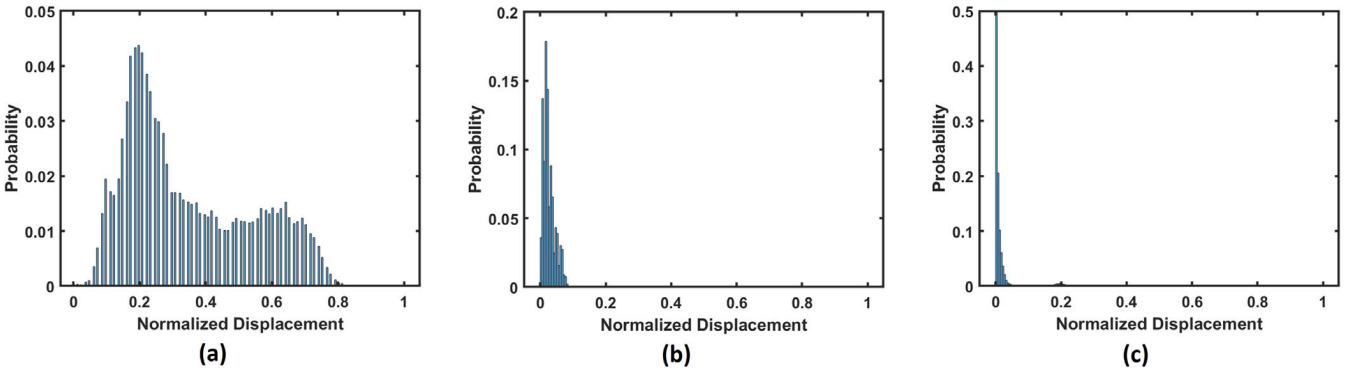

FIGURE 4. PMF of the experimentally obtained initial RF data for (a) 5 MHz tissue mimicking phantom, (b) 10 MHz tissue mimicking phantom, and (c) 5 MHz bovine eye tests.

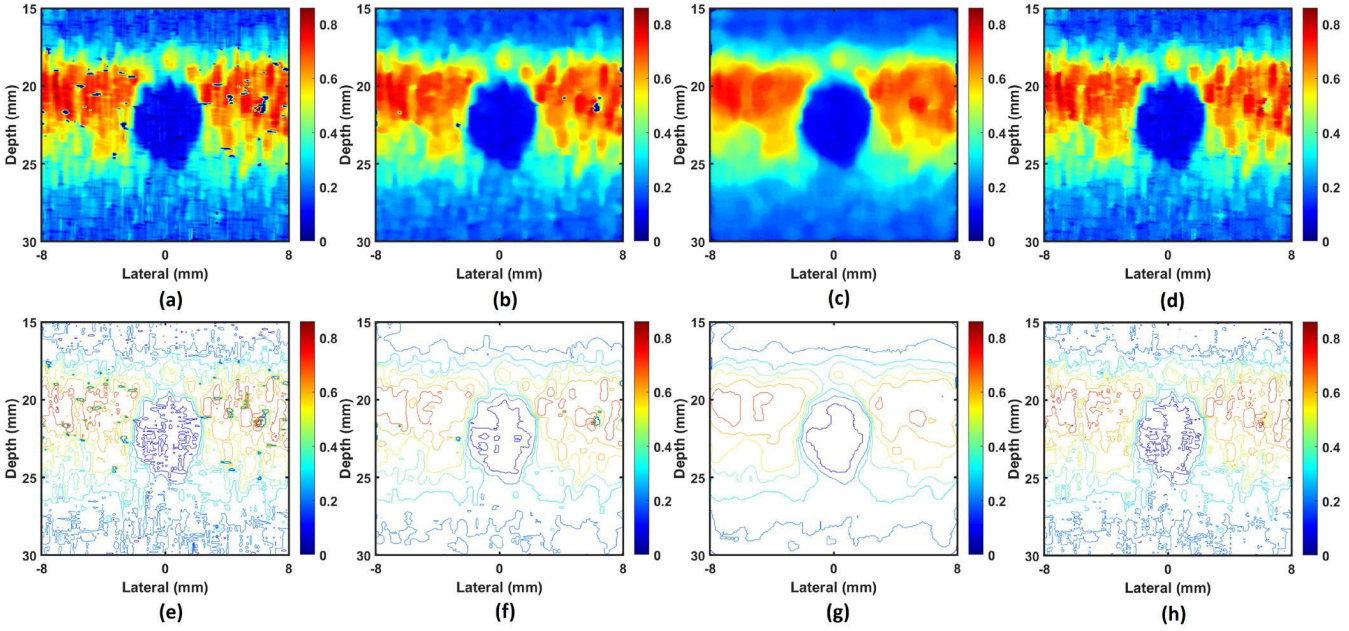

FIGURE 5. Experimentally obtained 5 MHz ARFI images and contour plots for a tissue mimicking phantom: ARFI images of (a) initial data, (b) FMF (5 × 5), (c) FMF (11 × 11), (d) proposed PMF_AMF (5 × 5 => 11 × 11); Contour plots of (e) initial data, (f) FMF (5 × 5), (g) FMF (11 × 11), and (h) proposed PMF_AMF (5 × 5 => 11 × 11). A color bar indicates normalized displacement.

D. ACQUISITION OF ARFI IMAGE DATA

Fig. 3(a) shows a tissue-mimicking cyst phantom fabricated using an agar. A cyst region with a diameter of 5 mm was made with an agar solution of 2.5% concentration and located in the center of the phantom. In the case of the background region, it was made with an agar solution of 0.6% concentration which has relatively lower stiffness than the cyst region. The same tissue-mimicking phantom was used for 5 MHz and 10 MHz transducers. The cyst was positioned 10 mm from the surface, considering the focal depths of 20 mm and 10 mm for the 5 MHz and 10 MHz transducers.

To obtain a 5MHz ARFI image, a beam sequence consisting of one reference beam with a 2-cycle sine wave, one pushing beam with a 1000-cycle sine wave, and 10 tracking beams with a 2-cycle sine wave was programmed using MATLAB (The MathWorks, Natick, MA, USA). In particular, to obtain the local target displacement, the pulse repetition frequency (PRF) of the 10 tracking beams was set to 10 KHz. In the case of 10 MHz ARFI imaging, all conditions of the beam sequence were the same as the 5 MHz case, except for the center frequency (10 MHz).

These programmed beam sequences are generated through a function generator (33600A, Keysight Technologies, Santa Clara, CA, USA) and amplified through an RF power amplifier (75A250, Amplifier Research, Souderton, PA, USA), and then applied to the transducer. The echo data was acquired by the pulser-receiver system (5073PR, Olympus NDT, MA, USA) and finally stored on the data acquisition (DAQ) board (CS121G2, GaGe Applied Technologies Inc., Lachine, QC, Canada). The lateral movement of the transducer for obtaining scanlines was controlled through a linear motor system (SHOT-304GS, SIGMA KOKI, Tokyo, Japan) with

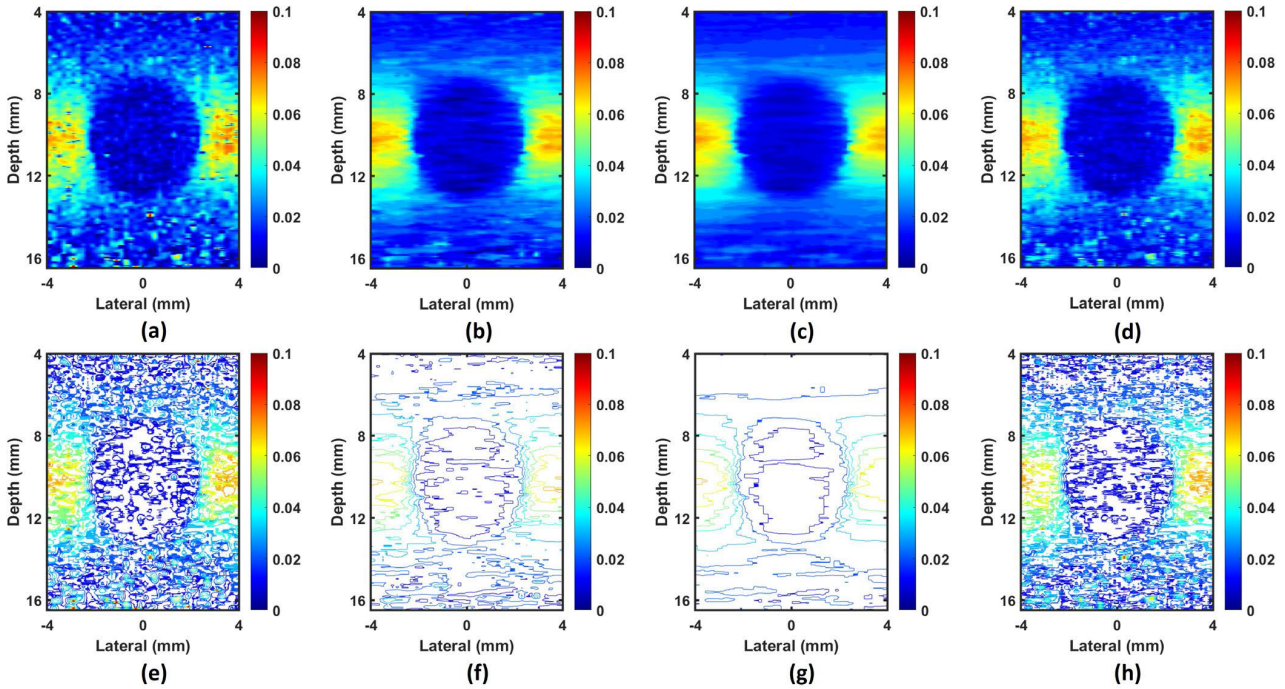

FIGURE 6. Experimentally obtained 10 MHz ARFI images and contour plots for a tissue mimicking phantom: ARFI images of (a) initial data, (b) FMF (5 × 5), (c) FMF (11 × 11), (d) proposed PMF_AMF (5 × 5 => 11 × 11); Contour plots of (e) initial data, (f) FMF (5 × 5), (g) FMF (11 × 11), and (h) proposed PMF_AMF (5 × 5 => 11 × 11). A color bar indicates normalized displacement.

LabVIEW (National Instruments. Austin, TX, USA) program. Fig. 3(c) shows the brightness mode (B-mode) image of the tissue mimicking phantom using the 5 MHz transducer. In the case of the bovine eye experiment as shown in Fig. 3(b), the experimental setup was similar to the tissue mimicking phantom, and the bovine eye was purchased commercially. Fig. 3(d) shows the B-mode image of the bovine eye.

III. RESULTS

A. INITIAL PMF OF TISSUE MIMICKING PHANTOM AND BOVINE EYE

Fig. 4 shows the initial PMF of the RF data for 5 MHz and 10 MHz tissue mimicking phantoms, and the 5 MHz bovine eye. Based on the algorithm as shown in Fig. 2, the initial data was modified. In Fig. 4(a), most normalized displacement was focused on by 0.86. This indicates that more than 0.86, that information may be the impulse noise rather than true displacement of the tissue. Thus, 0.86 will be a threshold cut-off level to distinguish them in the 5 MHz phantom. Fig. 4(b) shows the 10 MHz tissue mimicking phantom, and the cut-off level was 0.1. Fig. 4(c) shows the 5 MHz bovine eye and 0.1 was selected as the cut-off level. For a fair comparison, we also applied the thresholded data to the FMFs and compared their performance with the proposed method.

B. ARFI IMAGES OF TISSUE MIMICKING PHANTOM AND BOVINE EYE

Fig. 5 shows the ARFI images and their contour plots of the tissue mimicking phantom by using the 5 MHz transducer. Fig. 5(a) and (e) show the initial data before applying the FMF, where partially blue dots (artifact noise) are found in both the ARFI image and the contour plot. Fig. 5(b) and (f) show the results of applying the FMF with a kernel size of 5 × 5, and Fig. 5(c) and (g) show the results of applying the FMF with a kernel size of 11 × 11. Fig. 5(d) and (h) show the results of applying the PMF_AMF with a minimum kernel size of 5 × 5 and a maximum kernel size of 11 × 11. In the case of Fig. 5(b) and (f), compared to Fig. 5(c) and (g), various displacements appear, maintaining details but not partially removing noise. In Fig. 5(c) and (g), it can be seen that the filtering effect is large and consists of a narrow displacement range compared to other cases. On the other hand, Fig. 5(d) and (h) show that the noise of the initial image was removed, and the displacement distribution and details (necessary information) remain similar to the initial image.

Fig. 6 shows the ARFI images and their contour plots of the tissue mimicking phantom by using the 10 MHz transducer. As shown in Fig. 6(a) and (e), the impulse noise (red dots) is partially found in the initial data. In Fig. 6(b) and (f) using the FMF with a kernel size of 5 × 5, Fig. 6(c) and (g) using the FMF with a kernel size of 11 × 11, the impulse noises are removed. However, comparing Fig. 6(a) and (e), it can be seen that the displacement range is narrow, resulting in an image with low resolution. Fig. 6(c) and (g) are filtered more heavily than Fig. 6(b) and (f), and thus, these features are more visible. On the other hand, Fig. 6(d) and (h) show the detail image information similar to the initial data as the noise is removed.

Fig. 7 shows the ARFI images and their contour plots of the bovine eye by using the 5 MHz transducer. Fig. 7(a)-(d) show

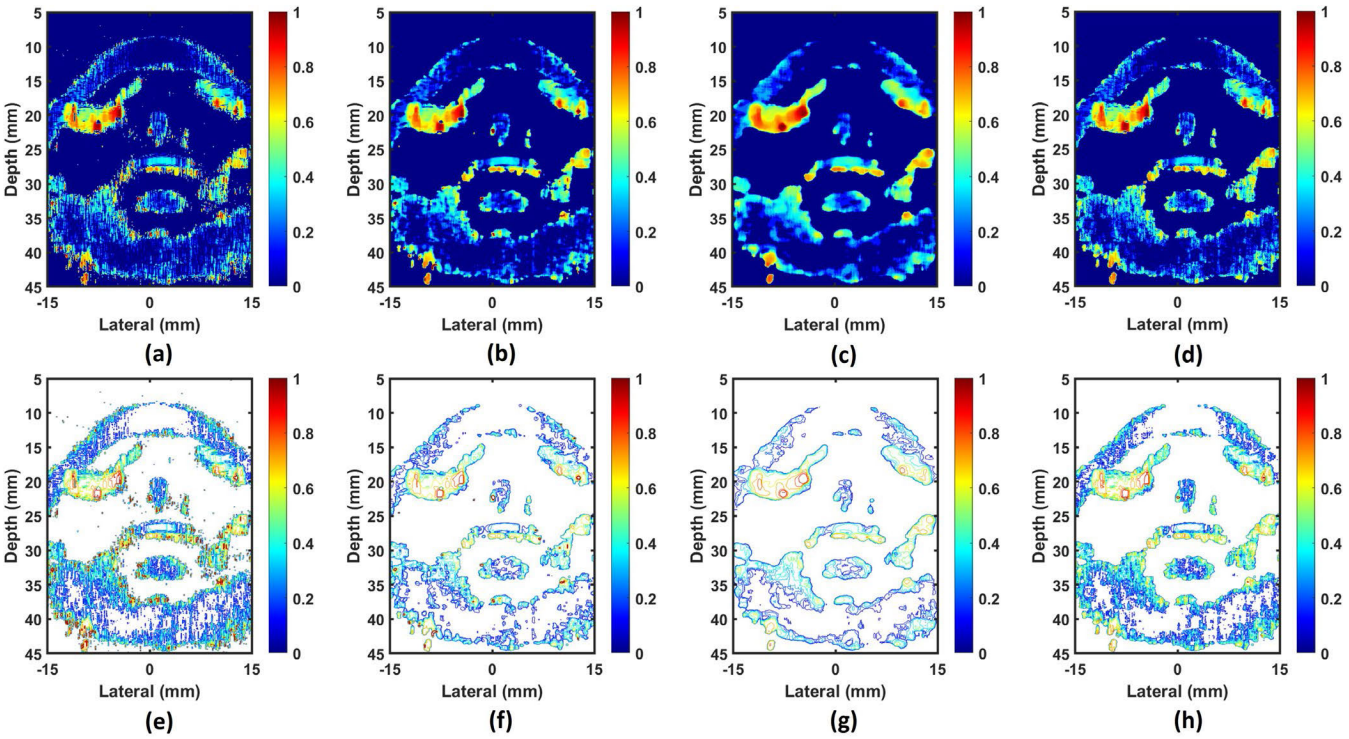

FIGURE 7. Experimentally obtained 5 MHz ARFI images and contour plots for a bovine eye: ARFI images of (a) initial data, (b) FMF (5 × 5), (c) FMF (11 × 11), (d) proposed PMF_AMF (5 × 5 => 11 × 11); Contour plots of (e) initial data, (f) FMF (5 × 5), (g) FMF (11 × 11), and (h) proposed PMF_AMF (5 × 5 => 11 × 11). A color bar indicates normalized displacement.

the ARFI images of the bovine eye based on the displacement value, and a logarithmic compression technique was applied because of the large dynamic range and the proportion of eye displacement values close to zero. Fig. 7(a) and (e) show the initial data before applying the FMF, where partially impulse noises (red dots) are found in both the ARFI image and the contour plot. In Fig. 7(b) and (f), the FMF with a kernel size of 5 × 5 was applied. In Fig. 7(c) and (g), the FMF with a kernel size of 11 × 11 was applied. Fig. 7(b) and (f) are composed of various displacements compared to Fig. 7(c) and (g), and thus, the detail image information is preserved, but some noises are not partially removed. In the case of Fig. 7(c) and (g), it can be seen that the filtering effect is large capable of removing the impulse noise but it provides a narrow range of displacements. On the other hand, Fig. 7(d) and (h) show a similar image pattern to the initial data as the noise is removed.

Fig. 8 shows the PMF of Fig. 5-7 as another method to check the performance of the proposed method. Fig. 8(a) shows the PMF of the initial data for the 5 MHz tissue-mimicking phantom, and Fig. 8(b) and (c) show the PMFs applied with the FMFs with kernel sizes of 5 × 5 and 11 × 11, respectively. Fig. 8(d) shows the PMF applied with the PMF_AMF technique with a minimum kernel size of 5 × 5 and a maximum kernel size of 11 × 11. It is found that the PMF distribution of the PMF_AMF is closer to that of the initial data compared to the FMF cases. Fig. 8(e) is the PMF of the initial RF data for the 10 MHz tissue mimicking phantom, and Fig. 8(f) and (g) show the PMFs applied with the FMFs with kernel sizes of 5 × 5 and 11 × 11, respectively. Fig. 8(h) shows the PMF applied with the PMF_AMF with a minimum kernel size of 5 × 5 and a maximum kernel size of 11 × 11. The PMF distribution of PMF_AMF is also closer to that of the initial data compared to the FMF cases. Fig. 8(i) is the PMF of the initial RF data of the 5 MHz bovine eye, and Fig. 8(j) and (k) show the PMFs applied with the FMFs with kernel sizes of 5 × 5 and 11 × 11, respectively. Fig. 8(l) shows the PMF applied with the PMF_AMF with a minimum kernel size of 5 × 5 and a maximum kernel size of 11 × 11. The PMF distribution of the PMF_AMF is closer to that of the initial data compared to the FMF cases.

Next, as shown in Fig. 9, the performance comparison between the proposed PMF_AMF and the AMF was also conducted using the bovine-eye data used in Fig. 7. When the AMF is used alone in the initial image that contains the impulse noise (Fig. 7(a)), the high amplitude impulse noise, which appears in the form of the spike-type red dot, remains in many parts of the ARFI image as shown in Fig. 9(a). This phenomenon can be seen more clearly in the 2D contour plot in Fig. 9(b) and in Fig. 9(c) where the two dimensional (2D) contour plot is converted to the three dimensional (3D) contour plot. As shown in Fig. 9(c), the spike-shaped parts shown in a dark-red color can be considered the impulse noise. On the other hand, applying the proposed PMF_AMF method to the same data shows that much of the impulse noise was removed as shown in Fig. 9(d). These results can also

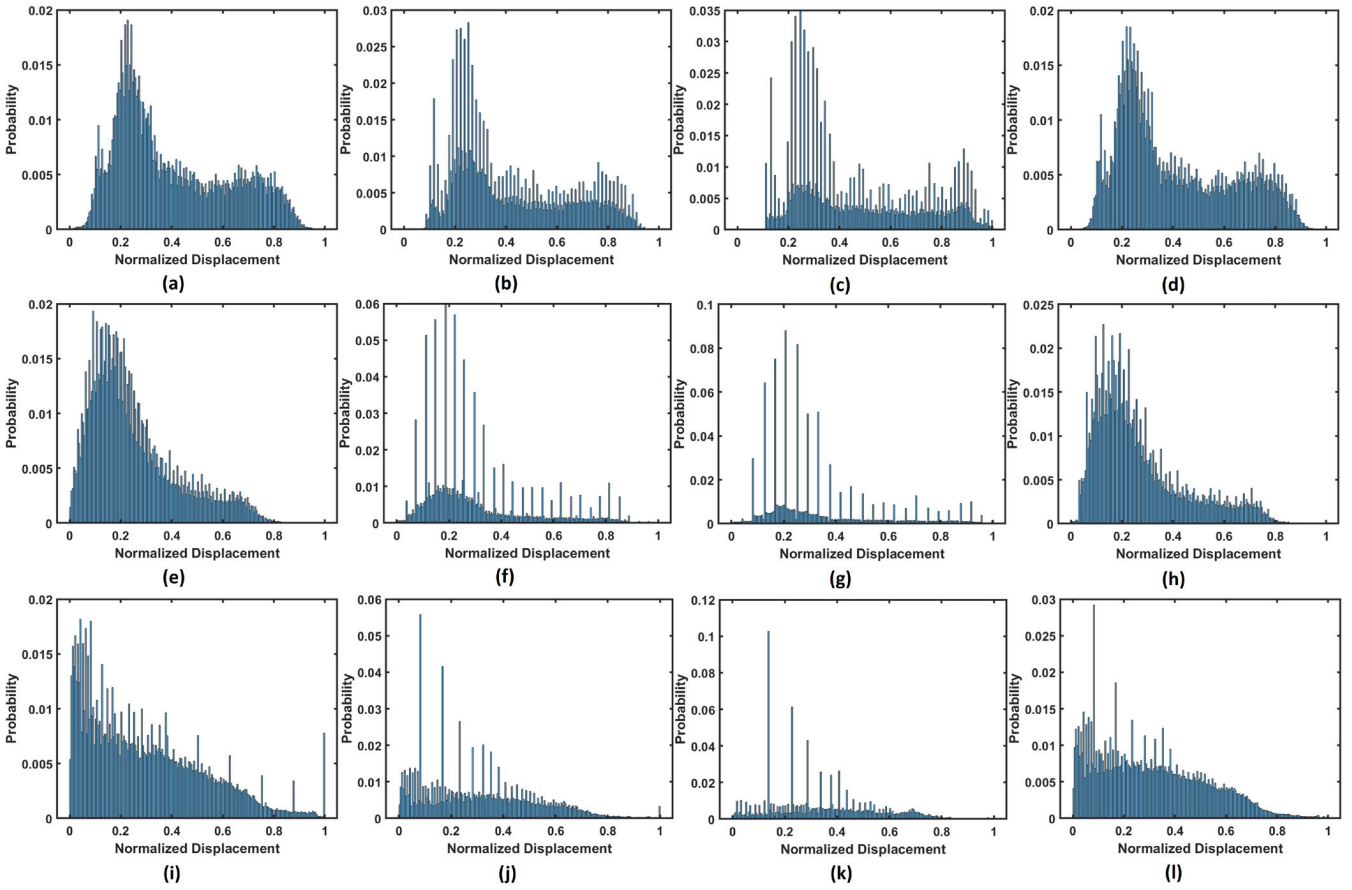

FIGURE 8. PMF of RF data: (a) initial data, (b) FMF (5 × 5), (c) FMF (11 × 11), (d) proposed PMF_AMF (5 × 5 => 11 × 11) for 5 MHz tissue mimicking phantom; (e) initial data, (f) FMF (5 × 5), (g) FMF (11 × 11), (h) proposed PMF_AMF (5 × 5 => 11 × 11) for 10 MHz tissue mimicking phantom; (i) initial data, (j) FMF (5 × 5), (k) FMF (11 × 11), (l) proposed PMF_AMF (5 × 5 => 11 × 11) for 5 MHz bovine eye.

be found on the 2D contour plot (Fig. 9(e)). In other words, the spiked-shaped impulse noise having a dark-red color was removed, and this can be clearly seen in the 3D contour plot in Fig. 9(f) compared to Fig. 9(d).

C. PERFORMANCE EVALUATION

A quantitative evaluation was performed through PSNR and SSIM. The PSNR values of the 5 MHz phantom were 72.88 dB for 5 × 5 FMF, 71.10 dB for 11 × 11 FMF, and 73.11 dB for the PMF_AMF. This means that the image of the PMF_AMF is most similar to the initial image, although the initial image has the impulse noises. The SSIM values of the 5 MHz phantom were 0.75 for 5 × 5 FMF, 0.57 for 11 × 11 FMF, and 0.87 for the PMF_AMF. This also means that the PMF_AMF image has very similar characteristics to the initial image. In the case of the 10 MHz phantom, the PSNR values were 88.48 dB for 5 × 5 FMF, 87.91 dB for 11 × 11 FMF, and 90.91 dB for the PMF_AMF. The SSIM values of the 10 MHz phantom were 0.92 for 5 × 5 FMF, 0.9 for 11 × 11 FMF, and 0.96 for the PMF_AMF. Thus, the PMF_AMF image is very similar to the initial image. In the case of 5 MHz bovine eyes, the PSNR values were 64.65 dB for 5 × 5 FMF, 63.61 dB for 11 × 11 FMF, and 65.68 dB for the PMF_AMF. The SSIM values of the 5 MHz bovine eye were 0.54 for 5 × 5 FMF, 0.48 for 11 × 11 FMF, and 0.70 for the PMF_AMF. This means that the PMF_AMF image is much more similar to the initial image than the FMF. Thus, the PMF_AMF image can be very similar to the initial image regardless of the target type. For the AMF alone case, a quantitative comparison with PMF_AMF by using PSNR and SSIM was not performed. This is because the ARFI image by using the AMF alone has still lots of impulse noises which is similar to the initial image having lots of impulse noises. For this reason, the PSNR and SSIM values of the AMF appear higher than those of the PMF_AMF. All PSNR and SSIM data are summarized in Table 1.

IV. DISCUSSION

In this study, we propose the probability mass function based adaptive median filter (PMF_AMF) to effectively remove the impulse noise from the acoustic radiation force impulse (ARFI) image. Generally, in the ARFI image, it is easy to occur the decorrelation error during the cross-correlation calculation process using data before and after compression, and the impulse noise (=false peak error) is one of the representative problems related to the decorrelation error. The artifact such as the decorrelation error in the ARFI image, especially the impulse noise, can introduce the abnormal change

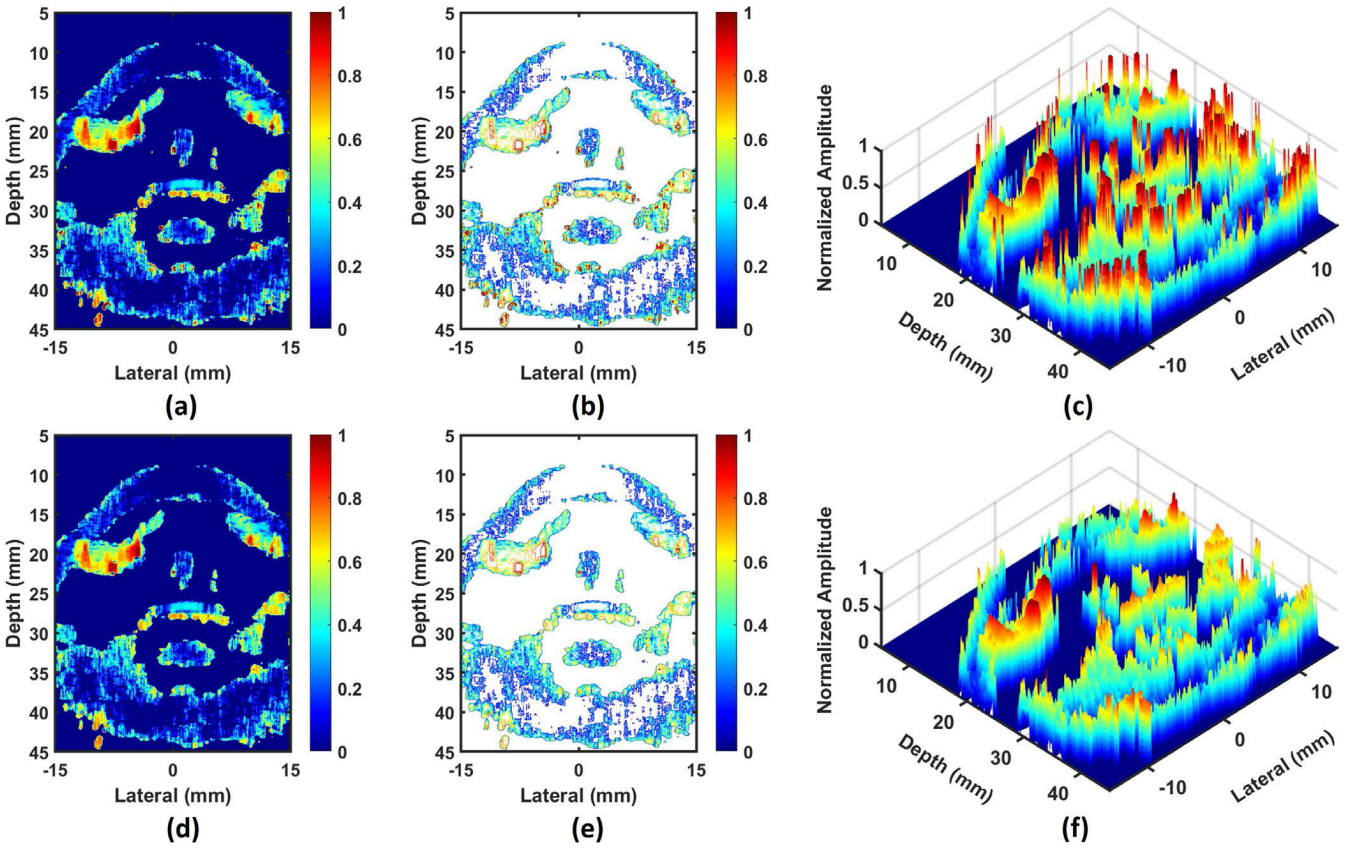

FIGURE 9. Performance comparison between AMF alone and PMF_AMF technique: (a) ARFI image, (b) 2D contour plot, and (c) 3D contour plot for AMF alone case; (d) ARFI image, (e) 2D contour plot, and (f) 3D contour plot for PMF_AMF case. A color bar indicates normalized displacement.

TABLE 1. Calculated PSNR and SSIM values obtained from tissue-mimicking phantom and bovine eye.

Targets	Procedure	PSNR (dB)	SSIM
5 MHz Tissue Mimicking Phantom	FMF (5 x 5)	72.88	0.75
	FMF (11 x 11)	71.10	0.57
	PMF_AMF (5 x 5 => 11 x 11)	73.11	0.87
10 MHz Tissue Mimicking Phantom	FMF (5 x 5)	88.48	0.92
	FMF (11 x 11)	87.91	0.90
	PMF_AMF (5 x 5 => 11 x 11)	90.91	0.96
5 MHz Bovine Eye	FMF (5 x 5)	64.65	0.54
	FMF (11 x 11)	63.61	0.48
	PMF_AMF (5 x 5 => 11 x 11)	65.68	0.70

in displacement measurement, which can lead to unreliable displacement estimation.

The fixed median filter (FMF) is a common tool used to eliminate the impulse noise, and it has been widely used for the ARFI imaging. However, it has a drawback of delivering inconsistent results depending on the noise density and causes an increase in the strain rate of the data by modifying all element values resulting in image distortion. In the case of tissue mimicking phantom and bovine eye experiments, there are lots of impulse noises (Fig. 5(a), Fig. 6(a), Fig. 7(a)). After using the FMF with a kernel size of 5×5, most impulse noises were disappeared, but some residual noises still remain due to the high noise density (Fig. 5(b), Fig. 6(b), Fig. 7(b)). If the kernel size is increased to 11×11, the residual noises were almost disappeared (Fig. 5(c), Fig. 6(c), Fig. 7(c)). However, the image resolution becomes low due to a blurred boundary of the target. This can be confirmed not only by ARFI images but also by contour plots. In particular, the contour plot clearly shows that the image contours between the initial data and the FMF data differ too much. On the other hand, the general AMF can effectively reduce the impulse noise while maintaining the detailed image information. This AMF is primarily effective in rejecting the impulse noise that is unipolar or bipolar in nature. Additionally, adjusting the kernel size helps mitigate the effects of the amplitude of the impulse noise. However, in the presence of different amplitudes and different types of the impulse noise, the performance of the AMF deteriorates. Therefore, in this study, the PMF, which has two roles, was used to enhance the effect of the AMF. The PMF is used to determine the cut-off level to effectively separate the displacement information and the impulse noise, and is used to limit the amplitude of the impulse noise. By applying the proposed PMF_AMF, residual noise was almost eliminated, and the resolution of the image was very similar to the initial image (Fig. 5(d), Fig. 6(d), Fig. 7(d)).

Fig. 5, Fig. 6, and Fig. 7 show the performance difference between the FMF method with different kernel size and the proposed PMF_AMF method. We also compared the performance between the AMF method alone and the PMF_AMF method by using the bovine-eye data. The results show that the PMF_AMF removed the impulse noise clearly compared to the AMF method alone as shown in Fig. 9. In other words, for the conventional AMF, if the kernel has two or more impulse noises of different amplitudes, a problem arises at level B (Fig. 2) due to the varying amplitudes of the impulse noises. In this case, although I_{xy} has a high value as the impulse noise, its amplitude is not equivalent to I_{max}. Thus, at Level-B, I_{xy} retains its I_{xy} value instead of replacing it to I_{med}. That is, the impulse noise represented by I_{xy} remains unremoved (Fig. 9(a)). On the other hand, by utilizing PMF_AMF, which applies a threshold based on the cut-off level set in PMF to limit the amplitude of impulse noise, the impulse noise that cannot be removed in Fig. 9(a) can be effectively removed as shown in Fig. 9(d).

Furthermore, the quantitative evaluation using PSNR and SSIM was conducted to compare the performance of the PMF_AMF compared to the FMF methods. The PMF_AMF method provides higher PSNR and SSIM values compared to the FMF with 5×5 and 11×11 kernel sizes, in both the tissue mimicking phantom and bovine eye experiments. This means that PMF_AMF, unlike FMF, has similar image characteristics to the initial image. In the AMF alone case, a quantitative comparison with PMF_AMF by using PSNR and SSIM was not performed. This is because the ARFI image by using the AMF alone has still lots of impulse noises which is similar to the initial image having lots of impulse noises. This phenomenon will increase the PSNR and SSIM values of the AMF alone case more than the PMF_AMF.

The method proposed in this paper has the advantage of efficiently removing the impulse noise and maintaining the image quality of the original image as much as possible. However, it is not easy to establish a standard for determining the threshold level based on PMF, and there is a possibility that it may be mixed with actual data information. Therefore, a further research using more diverse data that can overcome these limitations is needed. The deep learning-based image reconstruction method based on several algorithms can be a useful solution to solve this problem. Some research groups have been shown that the image reconstruction techniques play an important role in removing noises that occur during data collection in CT and MRI [33], [34], [35], [36]. In this case, it has been proven that the deep learning-based reconstruction methods can be used efficiently for the image reconstruction even with the limited data [35], [36]. In the future, additional research should be conducted to efficiently remove the impulse noise by combining the PMF_AMF method and the deep learning-based reconstruction technique. Additionally, due to the nature of AMF, it takes more calculation time than FMF, but this may not be a major problem as hardware performance has greatly improved.

V. CONCLUSION

In this study, the modified AMF based on the PMF is proposed. When applying the conventional AMF directly to the ARFI image, the impulse noise cannot be effectively removed. To solve this problem, the proposed method uses the PMF to block the impulse noise of the ARFI RF data as much as possible, and at the same time limits the amplitude of the impulse noise and then applies the AMF. As a result, it was confirmed that the resolution of the proposed method was very similar to the resolution of the initial image assuming no noise. In addition, unlike conventional methods using the image file, since the final image can be derived using the stored ultrasound RF data, it has the advantage of being directly applicable to a color image as well as a black and white image without an additional conversion process. Therefore, the proposed method is expected to be one of the useful ways to increase the resolution of the ARFI image.

REFERENCES

[1] W. Meng, G. Zhang, C. Wu, G. Wu, Y. Song, and Z. Lu, "Preliminary results of acoustic radiation force impulse (ARFI) ultrasound imaging of breast lesions," *Ultrasound Med. Biol.*, vol. 37, no. 9, pp. 1436–1443, Sep. 2011.

[2] J. R. Doherty, G. E. Trahey, K. R. Nightingale, and M. L. Palmeri, "Acoustic radiation force elasticity imaging in diagnostic ultrasound," *IEEE Trans. Ultrason., Ferroelectr., Freq. Control*, vol. 60, no. 4, pp. 685–701, Apr. 2013.

[3] R. S. Goertz, K. Amann, R. Heide, T. Bernatik, M. F. Neurath, and D. Strbel, "An abdominal and thyroid status with acoustic radiation force impulse elastometry—A feasibility study: Acoustic radiation force impulse elastometry of human organs," *Eur. J. Radiol.*, vol. 80, no. 3, pp. 226–230, 2011.

[4] C. Cassinotto, J. Boursier, V. de Lédinghen, J. Lebigot, B. Lapuyade, P. Cales, J. B. Hiriart, S. Michalak, B. L. Bail, V. Cartier, and A. Mouries, "Liver stiffness in nonalcoholic fatty liver disease: A comparison of supersonic shear imaging, FibroScan, and ARFI with liver biopsy," *Hepatology*, vol. 63, no. 6, pp. 1817–1827, 2016.

[5] Y. Lin, M. Yeh, C. Huang, J. Yang, P. Liang, C. Huang, C. Dai, Z. Lin, S. Chen, J. Huang, M. Yu, and W. Chuang, "The performance of acoustic radiation force impulse imaging in predicting liver fibrosis in chronic liver diseases," *Kaohsiung J. Med. Sci.*, vol. 32, no. 7, pp. 362–366, Jul. 2016.

[6] C. Bruno, S. Minniti, A. Bucci, and R. P. Mucelli, "ARFI: From basic principles to clinical applications in diffuse chronic disease-A review," *Insights Imag.*, vol. 7, no. 5, pp. 734–746, Oct. 2016.

[7] F. Kallel, T. Varghese, J. Ophir, and M. Bilgen, "The nonstationary strain filter in elastography: Part II. Lateral and elevational decorrelation," *Ultrasound Med. Biol.*, vol. 23, no. 9, pp. 1357–1369, Jan. 1997.

[8] M. F. Insana, L. T. Cook, and P. Chaturvedi, "Analytical study of bioelasticity ultrasound systems," in *Proc. 16th Int. Conf Inf. Process. Med. Imag.*, vol. 1999, pp. 1–14.

[9] W.-N. Lee, C. M. Ingrassia, S. D. Fung-Kee-Fung, K. D. Costa, J. W. Holmes, and E. E. Konofagou, "Theoretical quality assessment of myocardial elastography with in vivo validation," *IEEE Trans. Ultrason., Ferroelectr., Freq. Control*, vol. 54, no. 11, pp. 2233–2245, Nov. 2007.

[10] C. Pellot-Barakat, F. Frouin, M. F. Insana, and A. Herment, "Ultrasound elastography based on multiscale estimations of regularized displacement fields," *IEEE Trans. Med. Imag.*, vol. 23, no. 2, pp. 153–163, Feb. 2004.

[11] J. E. Lindop, G. M. Treece, A. H. Gee, and R. W. Prager, "3D elastography using freehand ultrasound," *Ultrasound Med. Biol.*, vol. 32, no. 4, pp. 529–545, Apr. 2006.

[12] J. Meunier and M. Bertrand, "Ultrasonic texture motion analysis: Theory and simulation," *IEEE Trans. Med. Imag.*, vol. 14, no. 2, pp. 293–300, Jun. 1995.

[13] S. Cui and D. C. Liu, "Noise reduction for ultrasonic elastography using transmit-side frequency compounding: A preliminary study," *IEEE Trans. Ultrason., Ferroelectr., Freq. Control*, vol. 58, no. 3, pp. 509–516, Mar. 2011.

[14] U. Bae and Y. Kim, "Angular strain estimation method for elastography," *IEEE Trans. Ultrason., Ferroelectr., Freq. Control*, vol. 54, no. 12, pp. 2653–2661, Dec. 2007.
[15] W. F. Walker and G. E. Trahey, "A fundamental limit on delay estimation using partially correlated speckle signals," *IEEE Trans. Ultrason., Ferroelectr., Freq. Control*, vol. 42, no. 2, pp. 301–308, Mar. 1995.
[16] R. Zahiri-Azar and S. E. Salcudean, "Motion estimation in ultrasound images using time domain cross correlation with prior estimates," *IEEE Trans. Biomed. Eng.*, vol. 53, no. 10, pp. 1990–2000, Oct. 2006.
[17] D. Zhang, M. Wan, D. Zhang, and H. Li, "False peak error removal using local difference median analysis in elastography," in *Proc. 3rd Int. Congr. Image Signal Process.*, vol. 9, Oct. 2010, pp. 4064–4068.
[18] T. Varghese and J. Ophir, "A theoretical framework for performance characterization of elastography: The strain filter," *IEEE Trans. Ultrason., Ferroelectr., Freq. Control*, vol. 44, no. 1, pp. 164–172, Jan. 1997.
[19] I. Pitas and A. Venetsanopoulos, "Nonlinear mean filters in image processing," *IEEE Trans. Acoust., Speech, Signal Process.*, vol. ASSP-34, no. 3, pp. 573–584, Jun. 1986.
[20] I. Pitas and A. N. Venetsanopoulos, *Nonlinear Digital Filters: Principles and Applications*. Norwell, MA, USA: Kluwer, 1990.
[21] S. Lal, S. Kumar, and M. Chandra, "Removal of high density salt & pepper noise through super mean filter for natural images," *Int. J. Comput. Sci. Issues*, vol. 9, no. 3, p. 303, May 2012.
[22] G. R. Arce, *Nonlinear Signal Processing: A Statistical Approach*. Hoboken, NJ, USA: Wiley, 2005.
[23] V. Gupta, D. K. Gandhi, and P. Yadav, "Removal of fixed value impulse noise using improved mean filter for image enhancement," in *Proc. Nirma Univ. Int. Conf. Eng. (NUiCONE)*, Nov. 2013, pp. 1–5.
[24] A. Sathesh and K. Rasitha, "A nonlinear adaptive median filtering based noise removal algorithm," in *Proc. 1st Int. Conf. Model., Control, Autom. Commun.*, 2010, pp. 108–113.
[25] S. Hetvi and S. Darshana, "Image restoration using adaptive median filtering," *Int. Res. J. Eng. IT Sci. Res.*, vol. 6, pp. 841–844, Oct. 2019.
[26] K. Nightingale, M. S. Soo, R. Nightingale, and G. Trahey, "Acoustic radiation force impulse imaging: In vivo demonstration of clinical feasibility," *Ultrasound Med. Biol.*, vol. 28, no. 2, pp. 227–235, Feb. 2002.
[27] E. Y. Jeong, J. H. Sung, and J. S. Jeong, "Improved acoustic radiation force impulse imaging using split-focused ultrasound transducer with phase inversion technique," *IEEE Sensors J.*, vol. 21, no. 2, pp. 1395–1403, Jan. 2021.
[28] M. A. Lubinski, S. Y. Emelianov, and M. O'Donnell, "Speckle tracking methods for ultrasonic elasticity imaging using short-time correlation," *IEEE Trans. Ultrason., Ferroelectr., Freq. Control*, vol. 46, no. 1, pp. 82–96, Jan. 1999.
[29] B. J. Fahey, K. R. Nightingale, R. C. Nelson, M. L. Palmeri, and G. E. Trahey, "Acoustic radiation force impulse imaging of the abdomen: Demonstration of feasibility and utility," *Ultrasound Med. Biol.*, vol. 31, no. 9, pp. 1185–1198, Sep. 2005.
[30] J. D. Allen, K. L. Ham, D. M. Dumont, B. Sileshi, G. E. Trahey, and J. J. Dahl, "The development and potential of acoustic radiation force impulse (ARFI) imaging for carotid artery plaque characterization," *Vascular Med.*, vol. 16, no. 4, pp. 302–311, Aug. 2011.
[31] R. Souchon, "Ultrasonic elastography," in *Physics for Medical Imaging Applications* (NATO Science Series), vol. 240, Y. Lemoigne, A. Caner, and G. Rahal, Eds. Dordrecht, The Netherlands: Springer, 2007, pp. 197–209, doi: 10.1007/978-1-4020-5653-6_15.
[32] G. Ye, J. A. Noble, P. P. Smith, and C. Hsieh, "A model-based displacement outlier removal algorithm for ultrasonic temperature estimation," in *Proc. IEEE Ultrason. Symp.*, n2008, pp. 2080–2083.
[33] K. Müller, A. K. Maier, C. Schwemmer, G. Lauritsch, S. De Buck, J.-Y. Wielandts, J. Hornegger, and R. Fahrig, "Image artefact propagation in motion estimation and reconstruction in interventional cardiac C-arm CT," *Phys. Med. Biol.*, vol. 59, no. 12, pp. 3121–3138, Jun. 2014.
[34] D. Li, Z. Bian, S. Li, J. He, D. Zeng, and J. Ma, "Noise characteristics modeled unsupervised network for robust CT image reconstruction," *IEEE Trans. Med. Imag.*, vol. 41, no. 12, pp. 3849–3861, Dec. 2022.
[35] W. Wu, D. Hu, C. Niu, H. Yu, V. Vardhanabhuti, and G. Wang, "DRONE: Dual-domain residual-based optimization network for sparse-view CT reconstruction," *IEEE Trans. Med. Imag.*, vol. 40, no. 11, pp. 3002–3014, Nov. 2021.
[36] W. Wu, Y. Wang, Q. Liu, G. Wang, and J. Zhang, "Wavelet-improved score-based generative model for medical imaging," *IEEE Trans. Med. Imag.*, early access, Oct. 19, 2023, doi: 10.1109/TMI.2023.3325824.

GA YEONG LEE (Student Member, IEEE) received the B.S. degree from the Department of Biomedical Engineering, Dongguk University, Seoul, South Korea, in 2023, where she is currently pursuing the M.S. degree. Her current research interests include medical ultrasound transducers, and signal and image processing.

GYU LI RA (Student Member, IEEE) is currently pursuing the B.S. degree with the Department of Biomedical Engineering, Dongguk University, Seoul, South Korea. Her current research interests include medical ultrasound transducers, and signal and image processing.

GIL SU KIM (Student Member, IEEE) received the B.S. degree from the Department of Biomedical Engineering, Dongguk University, Seoul, South Korea, in 2022, where he is currently pursuing the M.S. degree. His current research interests include medical ultrasound transducer and acoustic radiation force impulse imaging.

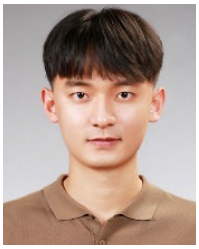

HAK HYUN MOON (Student Member, IEEE) received the B.S. degree from the Department of Biomedical Engineering, Dongguk University, Seoul, South Korea, in 2023, where he is currently pursuing the M.S. degree. His current research interests include medical ultrasound transducer and acoustic radiation force impulse imaging.

JONG SEOB JEONG (Member, IEEE) received the B.S. and M.S. degrees from the Department of Electronic Engineering, Sogang University, Seoul, South Korea, in 1999 and 2001, respectively, and the Ph.D. degree in biomedical engineering from the University of Southern California, Los Angeles, CA, USA, in 2010. From 2001 to 2005, he was with Samsung Electronics Company Ltd., Suwon, South Korea. From 2010 to 2011, he was a Postdoctoral Researcher with the NIH Resource Center for Medical Ultrasonic Transducer Technology, Department of Biomedical Engineering, University of Southern California. He is currently a Professor with the Department of Biomedical Engineering, Dongguk University, Seoul. His research interests include medical ultrasound signal processing and transducers for diagnosis and therapy.